Atomistic spin dynamics simulations of the MnAl τ-phase and its antiphase boundary

P. Nieves,[1,2,*] S. Arapan,[1,2] T. Schrefl,[3] and S. Cuesta-Lopez[1,2,†]

[1]*ICCRAM, International Research Center in Critical Raw Materials and Advanced Industrial Technologies,*
University of Burgos, 09001 Burgos, Spain
[2]*Advanced Materials, Nuclear Technology and NanoBioTechnology Department, University of Burgos, 09001 Burgos, Spain*
[3]*Center for Integrated Sensor Systems, Danube University Krems, 2700 Wiener Neustadt, Austria*

In this work we develop an atomistic spin dynamics model for the ideal $Mn_{50}Al_{50}$ τ-phase by means of first-principles calculations. The model is applied to study the domain wall and antiphase boundary phenomenology. In particular, it allows us to obtain the dependence on the interfacial exchange coupling of the nucleation and depinning fields, as well as the macroscopic magnetization profile across the antiphase boundary. We find that microscopic antiferromagnetic exchange coupling stronger than 10 meV could unavoidably lead to the formation of a domain wall at the antiphase boundary.

I. INTRODUCTION

Since the discovery of the MnAl τ-phase [1,2], extensive research has been done on this promising permanent magnet. This phase has a $L1_0$ structure and forms in a range of compositions stretching from 51 to 59 at.% Mn. It exhibits interesting properties such as high Curie temperature ($T_C = 650$ K), moderate saturation magnetization ($\mu_0 M_S = 0.75$ T), high uniaxial anisotropy ($K_u = 1.7$ MJ/m^3), and very low cost ($\sim$\$4/kg). Presently, it is cheaper than other interesting uniaxial Mn-based compounds such as MnBi, Mn_2Ga, Mn_3Ga, and Mn_3Ge [3]. It is also an attractive future alternative to expensive high-performance rare-earth permanent magnets because it does not contain critical raw materials. Moreover, the theoretical maximum-energy product $(BH)_{max}$ of 110 kJ/m^3 and theoretically expected coercivity $H_c \geqslant 800$ kA/m places the Mn-Al alloys far above the ferrite and Alnico magnets in the performance scale. However, the present main problems of this phase for permanent magnet applications are its metastable nature and moderate achieved coercivity in fully developed manufacturing methods ($H_c = 0.24$ MA/m) [4].

Usually, it exhibits a planar defect called an antiphase boundary (APB), which separates two regions where Mn and Al atoms interchange their sites in the MnAl τ-phase. Electron microscopy studies revealed strongly pinned magnetic domain walls at these APBs, probably due to an antiferromagnetic coupling between Mn atoms across it [5]. Frequently, a 180° magnetic domain wall with very narrow width (around one lattice spacing) is observed on each APB [6–9]. They also act as nucleation sites, which may decrease the coercivity [7]. However, further detailed studies of the atomic structure of this planar defect are still necessary to fully understand its possible role in the hysteresis behavior of the MnAl τ-phase [10].

Concerning to theoretical works on the MnAl τ-phase, first-principles calculations [11] indicated a noncollinear magnetic ground state in this compound with possible implications for the achievable M_S and $(BH)_{max}$. Young and Jakubovics developed a theory to explain the antiferromagnetic coupling at the APB of MnAl based on a Ruderman-Kittel interaction, finding that a hopping integral across the defect larger than the perfect crystal value can lead to a reversal of magnetization across the APB [12]. At mesoscopic level, Zijlstra derived a theoretical model to explain the strong pinning and nucleation of domain walls at the APB of the MnAl τ-phase [13]. Berger *et al.* performed Monte Carlo simulations in a ferromagnetic cylinder containing an APB, showing that the antiferromagnetic coupling across the APB could lead to a progressive rotation of spins with the formations of two "half" domain walls at the boundary with opposite chirality [14]. Recently, Bance *et al.* studied the APB of MnAl using micromagnetic simulations, confirming the relation between the antiferromagnetic coupling across the ABP and domain wall nucleation and pinning processes [15].

The MnAl τ-phase and its APB phenomenology have not been intensively studied by means of atomistic spin dynamics (ASD) simulations yet. ASD models are widely used as an intermediate tool connecting atomistic scales (usually study by first principles at 0 K) to micrometer scales (described by micromagnetics) in multiscale modeling of magnetic materials [16,17]. In particular, ASD simulations to compute the temperature dependence of some important properties such as equilibrium magnetization, anisotropy, exchange stiffness, etc., which are included in the micromagnetic approach. Additionally, ASD can provide a deeper understanding of microscopic spin dynamics close to defects, like APBs, and its dependence on the local magnetic properties. This information can be used in the design and optimization of a proper microstructure supporting high H_c.

In this work we develop an ASD model [18–20] of the ideal $Mn_{50}Al_{50}$ at.% τ-phase, and we apply it to study its domain wall and APB phenomenology. In Sec. II density functional theory (DFT) methods are used to calculate bulk and APB intrinsic properties. In Sec. III we make use of these microscopic parameters to construct an ASD model of this phase. In Sec. III A we compute the dependence on temperature of the domain wall width, anisotropy field, and exchange stiffness provided by this framework. In Sec. III B we calculate critical depinning and nucleation fields as a function of the exchange coupling at the APB. Finally, in Sec. IV we present the main conclusions of this work.
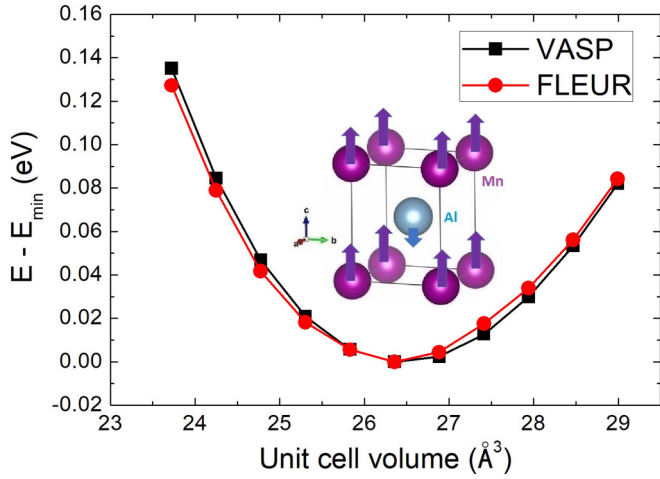
———————
*Corresponding author: pnieves@ubu.es
†scuesta@ubu.es

FIG. 1. Energy versus volume of the $Mn_{50}Al_{50}$ τ-phase assuming a collinear magnetic state obtained with the VASP and FLEUR codes. The minimum energy E_{min} was subtracted from the total energy. The inset shows the unit-cell structure of the $Mn_{50}Al_{50}$ τ-phase in the collinear state.

FIG. 2. Magnetocrystalline energy $\triangle E_{cell}(\theta,\phi) = E_{cell}(\theta,0) - E_{cell}(0,0)$ versus θ for the $Mn_{50}Al_{50}$ τ-phase. (θ,ϕ) stands for the direction where the total magnetization of the cell is constrained. Circles represent data calculated by DFT, and the line represents the function $E_{cell} = K_u \sin^2\theta$, with $K_u = 1.51 MJ/m^3$. The inset shows the energy cell difference $\triangle E_{cell}(\theta,\phi) = E_{cell}(\pi/2,0) - E_{cell}(0,0)$ versus the total number of k points used in the calculation.

II. FIRST-PRINCIPLES CALCULATIONS

A. Bulk

Recent improvements in the reproducibility and precision in the DFT Perdew-Burke-Ernzerhof (PBE) [21] functional framework open the possibility of combining results from different DFT codes in a consistent model [22]. Here, we calculate the required microscopic parameters of the $Mn_{50}Al_{50}$ at.% τ-phase for the development of an ASD model of it by means of DFT projector augmented-wave (PAW) and all-electron techniques. First, we calculated the energy of the unit cell at different cell volumes using the VASP code [23–26] and assuming a collinear magnetic state with potentials PAW PBE 5.4 [27], a Γ-centered Monkhorst-Pack k-point mesh (15×15×12) of the Brillouin zone (BZ), and an energy cutoff equal to 450 eV. This process was done with cell-volume relaxation for an initial estimation of the equilibrium volume, followed by cell-shape relaxation at different fixed cell volumes around the equilibrium volume. Figure 1 shows an energy versus unit-cell volume curve obtained with this procedure. The relaxed structure lowest in energy has lattice parameters $a = 2.755$ Å and $c/a = 1.26$, close to the experimental values ($a = 2.77$ Å and $c/a = 1.28$) [28]. The fitting of these data to the third-order Birch-Murnaghan equation of state leads to a bulk modulus of $B = 127.6$ GPa and $dB/dP = 4.0$. From the density of states at the collinear magnetic ground state along the z axis, we find the magnetic moments of Mn and Al, $\mu_{Mn,z} = 2.352\mu_B$ and $\mu_{Al,z} = -0.056\mu_B$, respectively. A similar value for the Mn magnetic moment was calculated in Ref. [11], $\mu_{Mn} = 2.42\mu_B$, using lattice parameters $a = 2.73$ Å and $c/a = 1.298$. The saturation magnetization reads $\mu_0 M_S(T = 0 \text{ K}) = 1.02$ T, which is larger than typical experimental values ($\sim$0.75 T) [3]. This deviation may be related to the antiferromagnetic alignment of the excess Mn atoms at the $1b$ site $(1/2,1/2,1/2)$ in nonequiatomic stoichiometries, smaller Mn magnetic moment and likely a noncollinear ground state [11,29]. In Fig. 1 we also show that these results can be
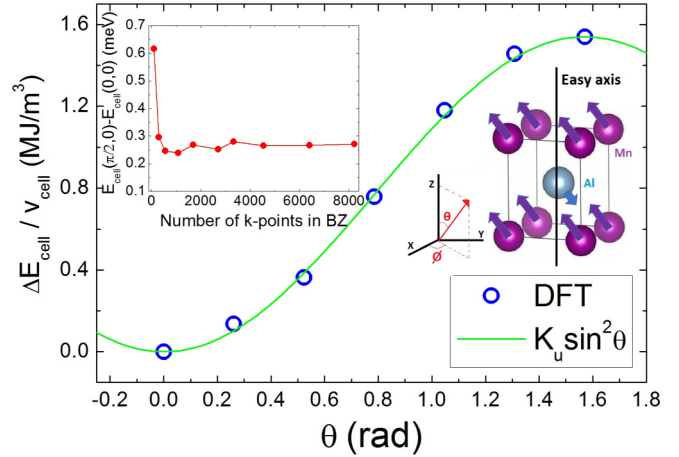
reproduced quite well using the FLEUR code [30,31] based on a full-potential augmented plane-wave method, where we used a Monkhorst-Pack k-point grid (15×15×12) of the BZ and a plane-wave cutoff of $k_{max} = 4.1$ a.u.$^{-1}$. The magnetic moments of the ground state given by this approach are $\mu_{Mn,z} = 2.35\mu_B$ and $\mu_{Al,z} = -0.07\mu_B$, while the bulk modulus is $B = 125.6$ GPa and $dB/dP = 4.0$, which compare well with the results given by VASP.

Next, we calculated the magnetocrystalline anisotropy of the $Mn_{50}Al_{50}$ τ-phase using the software VASP [23–26], where we took into account its spin-orbit coupling interaction. We used an automatic k-point mesh (15×15×12) of the BZ and an energy cutoff equal to 450 eV. In Fig. 2 we show the unit-cell energy change versus polar angle θ, where the unit-cell magnetization points to θ with an azimuthal angle $\phi = 0$. The inset shows the convergence test, where we present the energy difference $\triangle E_{cell}(\theta,\phi) = E_{cell}(\pi/2,0) - E_{cell}(0,0)$ versus the total number of k points in the BZ used in the calculation. We see that DFT data are quite close to the values given by the phenomenological curve $E_{cell}(\theta) = K_u \sin^2(\theta)$. The calculated uniaxial magnetocrystalline anisotropy is $K_u = 1.51 MJ/m^3$ at $T = 0$ K, which is in good agreement with previous DFT calculations [32]. The experimental value is about $K_u = 1.7 MJ/m^3$ [3].

Finally, we calculated the exchange integrals of the $Mn_{50}Al_{50}$ τ-phase using the FLEUR code. Namely, we used the frozen magnon calculations which employ the spin spiral formalism with 1089 k points in the irreducible Brillouin zone (IBZ), a plane-wave cutoff of $k_{max} = 4.1$ a.u.$^{-1}$, and 441 q points in the IBZ. The convergence was checked with respect to the above parameters. Figure 3 shows the calculated exchange parameters between Mn-Mn atoms, where the exchange energy is written as $E_{ex} = -\frac{1}{2}\sum_{i,j} J_{i,j}\mathbf{s}_i \cdot \mathbf{s}_j$, where $\mathbf{s}_i$ is the unit vector along the ith Mn atomic magnetic moment. We observe that exchange interactions beyond the
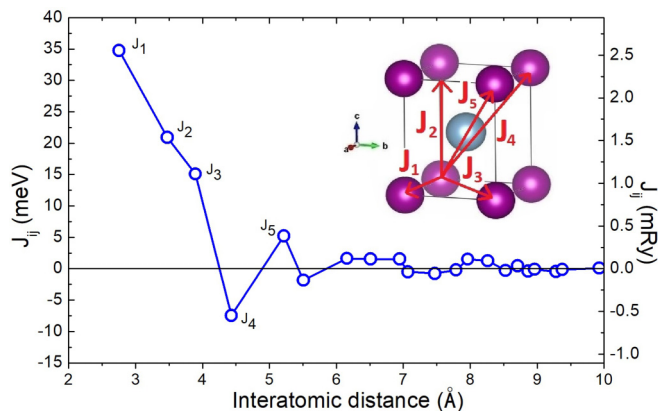
FIG. 3. Exchange integrals between Mn-Mn atoms in the $Mn_{0.5}Al_{0.5}$ τ-phase. The inset shows the exchange integrals up to the fifth nearest neighbor in the unit-cell structure of the $Mn_{50}Al_{50}$ τ-phase.

fifth nearest neighbor (n.n.) are quite small, so we will not include them in the ASD model. A summary of the calculated exchange parameters up to the fifth nearest neighbor (labeled by $J_{0,i} \equiv J_i, i = 1, \ldots ,5$) is presented in Table I. We also see that the overall interlayer ferromagnetic exchange coupling (mainly led by J_1 and J_3) is stronger than the intralayer one (mainly led by J_2, J_4, and J_5; see the inset in Fig. 3). This trend was also found in previous DFT calculations [11,33]. All exchange interactions between Al-Al and Mn-Al are very small in comparison with the strongest Mn-Mn ones. For example, the first-nearest-neighbor interactions between Al-Al and Mn-Al are -0.415 and 1.315 meV, respectively, so they are neglected in this ASD model. Both interactions are so weak mainly due to the very small magnetic moment of Al.

B. Antiphase boundary

The presence of an APB would alter the positions of Mn ions with respect to their positions in the ideal bulk MnAl.

TABLE I. Values of the parameters used in the ASD model for the $Mn_{50}Al_{50}$ at.% τ-phase.

Lattice parameters		
a (Å)	b (Å)	c (Å)
2.755	2.755	3.473

Magnetic moments		
$\mu_{Mn}(\mu_B)$	μ_{Al} (μ_B)	μ_{Mn}^{eff} (μ_B)
2.352	-0.056	2.296

Magnetocrystalline anisotropy
k_{Mn}^{eff} (J/atom)
39×10^{-24}

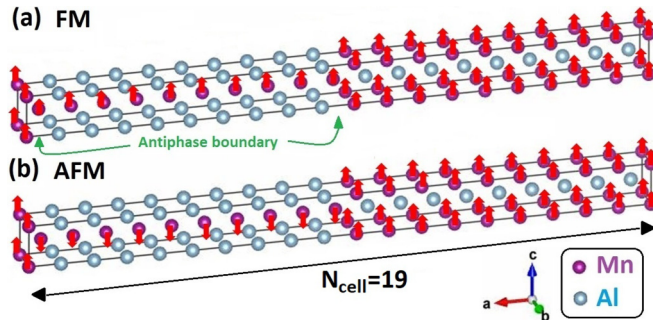| Exchange parameters			
i	$R_{0,i}$	n.n.	$J_{0,i}$ (meV)
1	(1,0,0)	4	34.749
2	(0,0,1)	2	20.926
3	(1,1,0)	4	15.089
4	(1,0,1)	8	-7.456
5	(1,1,1)	8	5.225

FIG. 4. (a) Ferromagnetic (FM) and (b) antiferromagnetic (AFM) collinear spin configurations across the APB of the MnAl τ-phase for a supercell of $19 \times 1 \times 1$ unit cells ($N_{cell} = 19$) along the X axis with periodic boundary conditions in the X, Y and Z axes. The equilibrium lattice parameters of each unit cell are also shown.

The change in positions will affect the magnetic properties in a region with relatively large atomic displacements. In this section we investigate the effect of the APB on the atoms in the vicinity of the interface for both the ferromagnetic (FM) and antiferromagnetic (AFM) collinear spin configurations across the APB by performing supercell calculations. An ideal APB system is modeled by an $N_{cell} \times 1 \times 1$ supercell (SC), where N_{cell} is the number of bulk MnAl unit cells. The APB is obtained by shifting half of the SC atoms by $(0, a/2, c/2)$. Due to the periodic boundary conditions there are, in fact, two APBs separated by half of the SC size along the x axis. The larger the separation is, the smaller the interaction is between both APBs inside the SC, and thus, the properties of a single APB can be estimated in the limit of a sufficiently large SC, as well as the trends in going from smaller to larger SCs.

We have performed DFT calculations for a set of SCs with $N_{cell} = 9, 11, 13, \ldots ,25$ modeling both types of FM and AFM APBs. For the FM APB spins on Mn atoms point in the same direction in both halves of the SC, while in the case of the AFM APB, spins on Mn atoms in one half of the SC point in the opposite direction with respect to the spins in the other half of the SC. In Fig. 4 we show a diagram of these configurations for a $19 \times 1 \times 1$ supercell. The AFM configuration corresponds to a domain wall with a width equal to one lattice spacing, frequently observed in experimental images of the APB in MnAl [6,7]. Calculations were done with the VASP code, and to study the effect of the APB on the bulk atomic positions, we allowed the atomic positions to relax, keeping fixed the volume and shape of the SC. The reason is that an infinitely large SC should describe bulk MnAl with a perfect APB plane. We used the PAW PBE 5.4 potentials and a density of k points similar to the bulk case, with a Γ-centered k-point mesh of $1 \times 15 \times 11$.

We first analyzed the interatomic distances and magnetic moments on Mn atoms in the region next to the APB. Taking as the origin a Mn atom across the interface we denote by $\mathbf{R}_n$ the positions of Mn atoms in the other half of the APB system, as shown in the graphical representation of the SC at the top of Fig. 5. We can see that interatomic distances are more affected in the AFM APB, with a relatively large deviation from the bulk case for the atoms in the next-nearest region of the APB interface. The reason is that a stronger
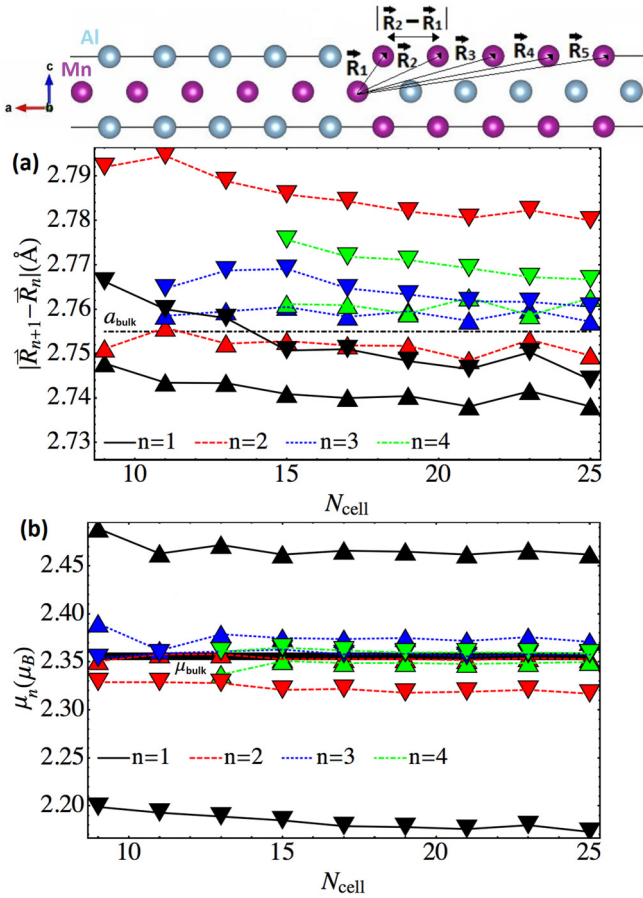
FIG. 5. (a) Atomic distance between Mn-Mn atoms and (b) Mn atomic magnetic moment at position $\mathbf{R}_n$ as a function of supercell size. Position vectors $\mathbf{R}_n$ are shown in the diagram at the top. Upward and downward triangles stand for FM and AFM spin configurations across the APB, respectively. In (a) the black dash-dotted line represents the lattice parameter a_{bulk} of the bulk MnAl τ-phase, while in (b) it stands for the Mn atomic magnetic moment of the bulk MnAl τ-phase.

AFM interaction pulls Mn atoms at the interface closer to each other. Due to the presence of two interfaces this results in an increased separation between atoms at positions $\mathbf{R}_3$ and $\mathbf{R}_4$. We also observe that considerable changes occur mainly within the first two to three units cell from the interface, and beyond this region the interatomic distances tend to their bulk values. As for the magnetic moment, it is less susceptible to the SC size and changes only for Mn atoms at the interface. The change in the magnetic moment at the interface is also dependent on the type of APB, increasing for the ferromagnetic interaction across the APB and decreasing for the antiferromagnetic one.

Next, we analyze the charge density close to the APB for FM and AFM configurations. In Fig. 6 we show the charge-density isosurface equals $0.0418\,e/\text{bohr}^3$ for FM and AFM spin configurations across the APB in the $19\times1\times1$ supercell. We see that charge density becomes quite similar to the bulk beyond the second unit cell next to the APB for both FM and AFM configurations. We also observe that charge density between Mn atoms at $(0,0,0)$ and $(1/2,1/2,1/2)$ across the APB is larger in the AFM configuration than in FM one. This fact can be better seen in Fig. 7(a), where
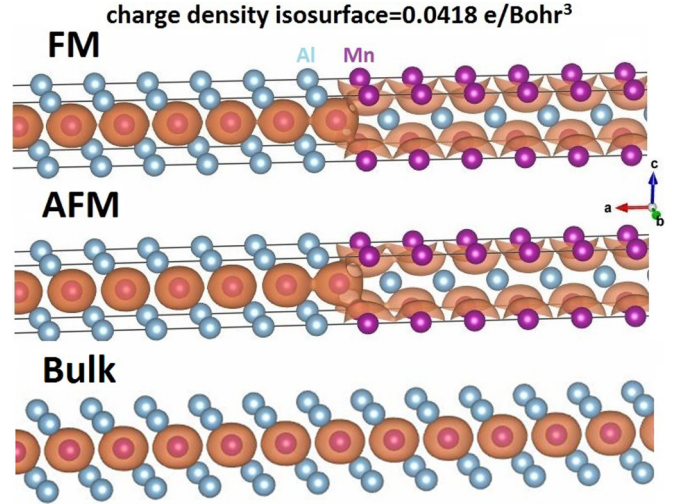

FIG. 6. Charge-density isosurface equals $0.0418\,e/\text{bohr}^3$ for FM (top) and AFM (middle) spin configurations across the APB in the $19\times1\times1$ supercell and $0.0418\,e/\text{bohr}^3$ for the FM collinear spin configuration in bulk (bottom).

a charge-density slice is plotted on the lattice plane across Mn atoms at $(0,0,0)$ and $(1/2,1/2,1/2)$, with Miller indices $(h,k,l) = (18.79,0,-1)$ for FM and $(h,k,l) = (20.48,0,-1)$ for AFM, in the APB for a $19\times1\times1$ supercell. Similarly, in Fig. 7(b) we present a charge-density slice on the lattice plane across Mn atoms at $(1/2,1/2,1/2)$, with Miller indices $(h,k,l) = (0,0,-1)$. Here, we see that there is a larger charge density between Mn atoms in the second and third unit cells next to the APB for the FM spin configuration than for the AFM one. These results suggest that the APB has a short-range effect on the microscopic properties of the atoms close to it.

Finally, the AFM configuration was lower in energy than the FM one in all calculated supercells, which may suggest
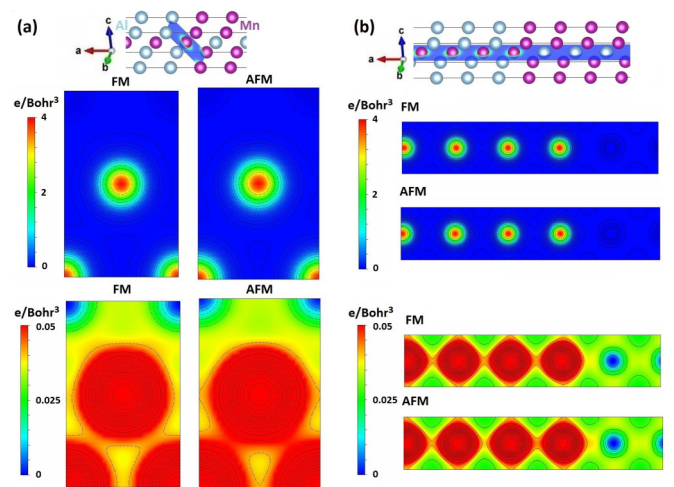

FIG. 7. Charge-density slices of the $19\times1\times1$ supercell at lattice planes: (a) $(h,k,l) = (18.79,0,-1)$ for FM and $(h,k,l) = (20.48,0,-1)$ for AFM spin configurations across the APB and (b) $(h,k,l) = (0,0,-1)$. These slices are shown in the diagram on the top.

an antiferromagnetic exchange coupling across the APB [5]. The strength of this interaction will be analyzed using first principles in a future work. Here, we set it as a free parameter in the ASD simulations of the APB, and we study the APB phenomenology as a function of its strength (see Sec. III B). The advantage of this procedure is that it can provide the dependence of the mesoscopic magnetization profile close to the APB, which might be observed experimentally, on the value of microscopic exchange coupling across it.

III. ATOMISTIC SPIN MODEL

In order to perform ASD simulations of the $Mn_{50}Al_{50}$ at.% τ-phase we consider an effective three-dimensional Heisenberg spin system in a tetragonal lattice with lattice parameters $a = 2.755$ Å and $c/a = 1.26$ ($v_{cell} = 26.358$ Å^3). Basically, from the point of view of ASD the main effect of Al atoms is to decrease slightly the total spin polarization of the unit cell. Hence, in this model we take into account such an effect by considering only Mn spins with an effective magnetic moment, which corresponds to the average magnetic moment of the unit cell at $T = 0$ K given by DFT calculations ($\mu_{Mn}^{eff} = \mu_{Mn} + \mu_{Al}$). Doing so, the effective ASD model gives the same saturation magnetization at $T = 0$ K as DFT calculations. These effective Mn localized magnetic moments are placed at Mn sites in the MnAl τ-phase. Similarly, we consider a uniaxial anisotropy of each effective Mn spin equal to $k_{Mn}^{eff} = 39.8 \times 10^{-24}$ J/atom, which corresponds to the value given by DFT calculations presented in Sec. II. Moreover, we include exchange parameters up to the fifth nearest neighbors. In Table I we present a summary of the value parameters used in the ASD model. The dynamics of each effective localized Mn magnetic moment μ_i is described by the stochastic Landau-Lifshitz-Gilbert equation [18,19]

$$\frac{d\mathbf{s}_i}{dt} = -\frac{\gamma}{1+\lambda^2}[\mathbf{s}_i \times \mathbf{B}_{eff,i} + \lambda \mathbf{s}_i \times (\mathbf{s}_i \times \mathbf{B}_{eff,i})], \quad (1)$$

where $\mathbf{s}_i = \mu_i/\mu_i$ is the normalized classical atomic magnetic moment, λ is the atomic coupling to the bath parameter, $\gamma = 1.76 \times 10^{11}$ T^{-1} s^{-1} is the gyromagnetic ratio, and $\mathbf{B}_{eff,i}$ is the effective field, given by

$$\mathbf{B}_{eff,i} = -\frac{\partial \mathcal{H}}{\partial \mu_i} + \mathbf{B}_{th,i}. \quad (2)$$

In this equation $\mathcal{H}$ is the Heisenberg spin Hamiltonian

$$\mathcal{H} = -\mu_0 \sum_i \mathbf{H} \cdot \mu_i - \sum_i k_i s_{i,z}^2 - \frac{1}{2} \sum_{i,j} J_{ij} \mathbf{s}_i \cdot \mathbf{s}_j, \quad (3)$$

where $\mathbf{B} = \mu_0 \mathbf{H}$ is the external magnetic field, μ_0 is the permeability of free space, k_i is the atomic uniaxial anisotropy constant, and J_{ij} is the exchange constant between atoms i and j. The second term in the effective field, Eq. (2), corresponds to the thermal field

$$\mathbf{B}_{th,i} = \mathbf{\Gamma}(t)\sqrt{\frac{2\lambda k_B T}{\gamma \mu_i \Delta t}}, \quad (4)$$

where k_B is the Boltzmann constant, T is the temperature, $\Delta t = 10^{-16}$ s is the integrator time step, and $\mathbf{\Gamma}(t)$ is a Gaussian distribution in three dimensions with a mean of zero. In the

simulations we set $\lambda = 1$ in order to reach equilibrium states rapidly.

In this work we are simulating small regions of a material (in the nanometer scale) which is supposed to be embedded in a much larger material (bulk). Hence, we cannot properly take into account the effect of dipole-dipole interactions (demagnetizing field) of the material in our ASD simulations. In the case of APB this interaction may play a relevant role because it could be sufficient to emit a domain wall [13]. Therefore, in order to estimate such an effect in ASD simulations of APB, we consider a demagnetizing field through macrocell approximation [19]. Namely, the system is discretized into macrocells with a fixed cell size ($5 \times 5 \times 5$ spins). The demagnetizing field on atomic magnetic moment μ_i inside macrocell p reads

$$\mathbf{B}_{demag,i}^p = \frac{\mu_0}{4\pi}\left[\sum_{q \neq p} \frac{3(\boldsymbol{m}_{mc}^q \cdot \hat{\boldsymbol{r}}_{pq})\hat{\boldsymbol{r}}_{pq} - \boldsymbol{m}_{mc}^q}{r_{pq}^3}\right]$$

$$+ \frac{\mu_0}{4\pi}\left[\sum_{j \neq i; j \in mc_p} \frac{3(\mu_j \cdot \hat{\boldsymbol{r}}_{ij})\hat{\boldsymbol{r}}_{ij} - \mu_j}{r_{ij}^3}\right], \quad (5)$$

where $\boldsymbol{m}_{mc}^q = \sum_{j \in mc_q} \mu_j$ is the total magnetic moment of macrocell q, $\hat{\boldsymbol{r}}_{pq}$ is the unit vector in the direction between the centers of macrocells p and q, and $\hat{\boldsymbol{r}}_{ij}$ is the unit vector in the direction between the atomic magnetic moments i and j. The first term in Eq. (5) approximately describes the demagnetizing field created by other macrocells on macrocell p, while the second term takes into account the exact local dipole-dipole interaction between atomic magnetic moments which belong to the same macrocell p. Computing this field is quite time-consuming for a large number of atomic magnetic moments, so here, it is updated every 10^4 time steps. Notice that time scales associated with the changes in the demagnetization field are typically much longer than Δt [19]. We include only demagnetizing fields in the ASD calculations of the APB in Sec. III B, not in the bulk (Sec. III A).

In Fig. 8 we show the magnetization versus temperature curve given by the ASD model for the MnAl τ-phase using a system size of $40 \times 40 \times 40$ spins. We obtain $T_C = 660$ K, which is very close to the experimental value $T_C^{exp} = 653$ K [2]. We compare these results with the experimental data on the $Mn_{55}Al_{45}$ at.% τ-phase in an external magnetic field of $\mu_0 H = 0.8$ T given in Ref. [34] and on the $Mn_{53.5}Al_{46.5}$ at.% τ-phase without external magnetic field given in Ref. [35] up to 300 K. Notice that the classical Heisenberg model leads to a temperature-dependent magnetization $m(T)$ described by the Langevin function, which typically is not fully in good agreement with experiments over the entire range of temperature, as we see in Fig. 8. The inset shows the Curie temperature as a function of the nearest-neighbor cutoff obtained by ASD simulations and mean-field approximation (MFA), $T_C^{MFA} = (1/3k_B)\sum_{\boldsymbol{R}} J_{0,\boldsymbol{R}}$. This calculation was done using the software UPPASD [18,36]. We see that T_C does not change too much, including nearest neighbors beyond the fifth ones. The T_C obtained by ASD for fourth-nearest-neighbor cutoff is not shown because it corresponds to an interlayer antiferromagnetic state.
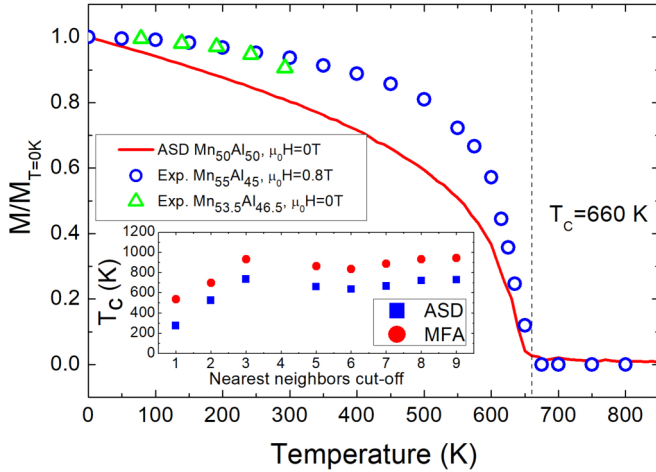
FIG. 8. Magnetization versus temperature given by the atomistic spin model for the $Mn_{50}Al_{50}$ at.% τ-phase (red line) and experiments on the $Mn_{55}Al_{45}$ at.% τ-phase in an external magnetic field of $\mu_0 H = 0.8$ T given in Ref. [34] (blue circles) and on the $Mn_{53.5}Al_{46.5}$ at.% τ-phase in an external magnetic field of $\mu_0 H = 0$ T given in Ref. [35] (green triangles). The inset shows the Curie temperature as a function of nearest neighbor cutoff.

A. Domain wall width and exchange stiffness

In this section we study the domain wall phenomenology using the ASD model of the MnAl τ-phase for a system with $300\times60\times60$ spins. The domain wall is simulated along the X axis, where the magnetization points along the easy axis (Z axis); periodic boundary conditions are used only in the Y and Z axes. We constrained Mn magnetic moments placed on the left and right sides of X-axis boundaries along the positive and negative Z-axis directions, respectively. As the initial starting configuration for domain wall simulations, we set Mn magnetic moments placed at negative and positive sites of the X axis along the positive and negative Z-axis directions, respectively. Figure 9 shows the domain wall profile at $T = 5$ K (a $180°$ Bloch wall) given by ASD simulations,
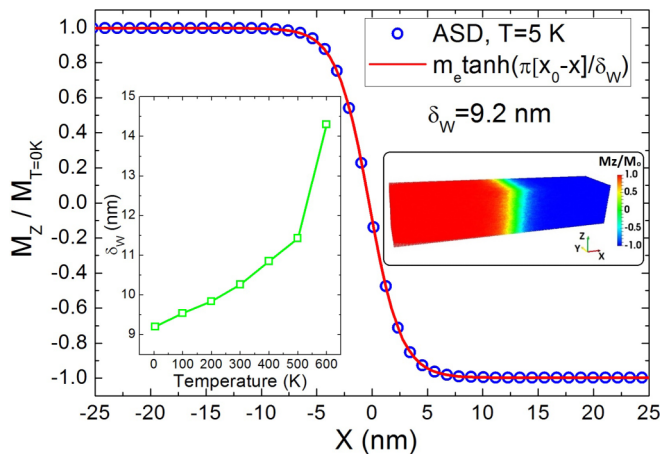

FIG. 9. Domain wall profile at $T = 5$ K. The inset on the left shows the domain wall width versus temperature, while the inset on the right shows the local z component of magnetization in the ASD model.
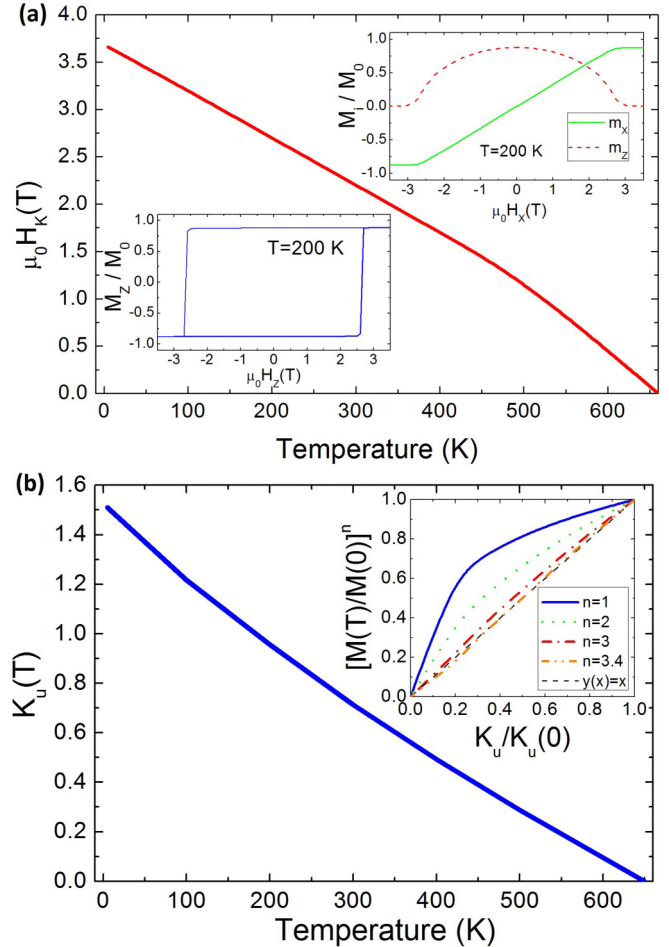

FIG. 10. (a) Anisotropy field $\mu_0 H_K$ versus temperature computed from hysteresis loops. Insets show hysteresis loops obtained by ASD simulations for external magnetic fields along the x and z axes at $T = 200$ K. (b) Temperature dependence of K_u calculated via $K_u(T) = \mu_0 M_s(0)m(T)H_K(T)/2$, where $m(T)$ and $H_K(T)$ are taken from the ASD data given in Figs. 8 and 10(a), respectively. The inset shows the ASD data $[M(T)/M(0)]^n$ versus $K_u(T)/K_u(0)$ for different Callen-Callen law exponents $n = 1, 2, 3,$ and 3.4.

where a domain wall width $\delta_w(T = 5$ K$) = 9.2$ nm is obtained. This value is calculated by fitting the domain wall profile to the function [37] $m_z(x) = m_e \tanh(\pi[x_0 - x]/\delta_w)$, where m_e, x_0, and δ_w are considered fitting parameters.

The calculated domain wall width at different temperatures is shown in the inset of Fig. 9, in which we see that δ_w increases linearly with temperature up to 500 K. Next, in order to compute the hysteresis loops we consider a smaller system made of $30\times30\times30$ spins with periodic boundary conditions. Figure 10(a) shows the anisotropy field H_K versus temperature obtained from ASD hysteresis loops. The anisotropy field is found to decrease linearly with temperature, in good agreement with experimental observations [38]. From these results we can compute the temperature dependence of the magnetocrystalline anisotropy using $K_u(T) = \mu_0 M_s(0)m(T)H_K(T)/2$, where $m(T)$ and $H_K(T)$ are taken from the ASD data given in Figs. 8 and 10(a), respectively. In Fig. 10(b) we present the results of the calculation of $K_u(T)$ using that procedure. In the inset of Fig. 10(b) we observe that the ASD data follow
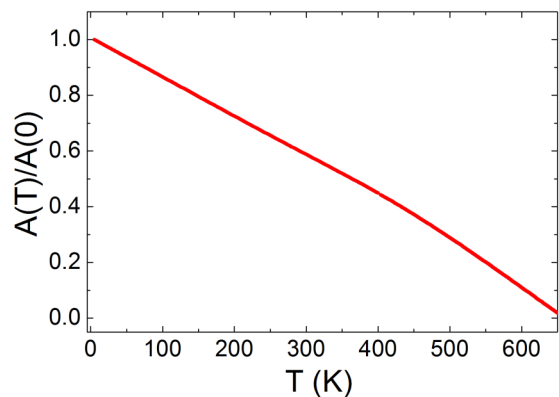
FIG. 11. Normalized exchange stiffness $A/A(0)$ versus temperature given by the ASD model.

the Callen-Callen law $K_u(T) \simeq K_u(0)[M(T)/M(0)]^n$ with $n = 3.4$, close to the $n = 3$ (single-ion anisotropy mechanism) obtained in experiments given in Ref. [35]. Recently, it was found that an exponent $n = 1$ could also describe the anisotropy temperature dependence in multilayer thin films [39].

Finally, from the well-known expression $\delta_w = \pi\sqrt{A/K_u}$, where A is the exchange stiffness parameter, and ASD results of $\delta_w(5K) = 9.2$ nm and $K_u(0) = 1.51$ MJ/m^3, we obtain $A(0) \simeq 12.95$ pJ/m. Notice that lower values of A and δ_w for the MnAl τ-phase were previously reported ($A \sim 3.2$–6.4 pJ/m, $\delta_w \sim 4.1$–10.9 nm) [40,41]. In Fig. 11 we present the calculated temperature dependence of $A(T)$ given by this ASD model using the expression $A(T) = [\delta_w(T)/\pi]^2 K_u(T)$, where $\delta_w(T)$ and $K_u(T)$ are taken from ASD data in Figs. 9 and 10(b), respectively. We see that $A(T)$ exhibits a large dependence on temperature mainly due to the
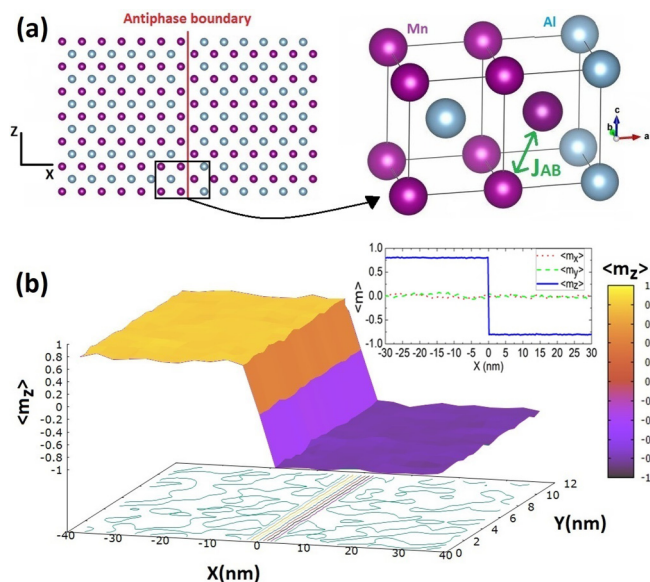

FIG. 12. (a) Schematic of the antiphase boundary for the Mn$_{50}$Al$_{50}$ τ-phase. (b) Antiphase boundary decorated with a domain wall. It was obtained by ASD simulations with $J_{AB} = -19$ meV at $T = 300$ K.
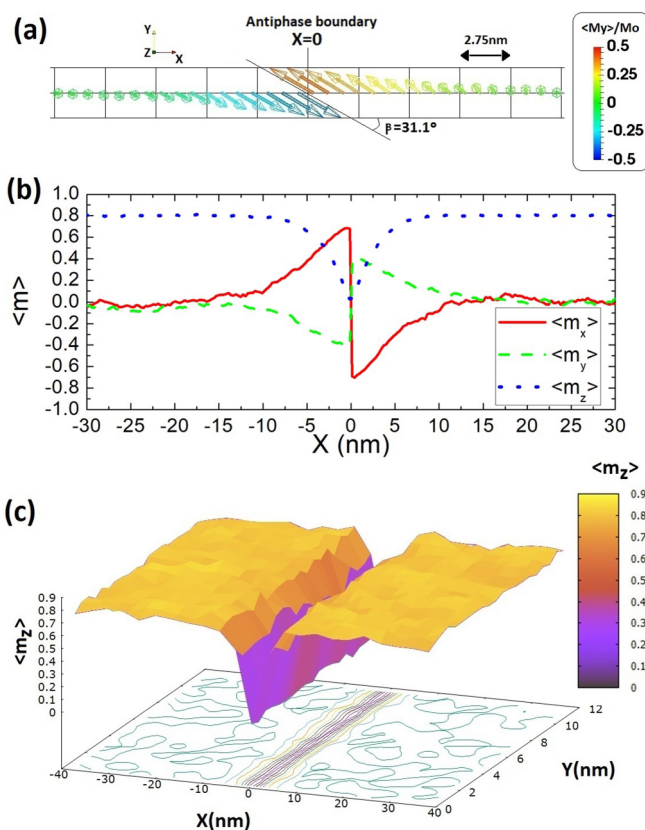

FIG. 13. (a) Spatial average magnetization vector, (b) magnetization components, and (c) magnetization z component across the APB using $J_{AB} = -19$ meV at $T = 300$ K without external magnetic field and demagnetizing field. As initial conditions we set the magnetization of both antiphases pointing to the positive direction of the Z axis (easy axis).

Langevin-like behavior of $M(T)/M(0)$ coming from the ASD simulations [42].

B. Antiphase boundary

Next, we apply the developed ASD model to study the APB phenomena in the MnAl τ-phase. To this end, we consider a system of $300 \times 50 \times 50$ spins (i.e., with lateral sizes $L_x = 82.7$ nm, $L_y = 13.8$ nm, and $L_z = 173.7$ nm), where an ideal APB is placed on the plane YZ at $x = 0$ [see Fig. 12(a)]. Periodic boundary conditions are used only in the Y and Z axes. In Sec. II B we found that changes in lattice parameters and magnetic moments close to APB are small in comparison to the bulk. Hence, we set bulklike lattice parameters and magnetic moments close to the APB in the ASD model. For the sake of simplicity we assume the same atomic magnetocrystalline anisotropy constant close to the APB as in the bulk. Concerning the exchange coupling across the APB, experimental observations such as strongly pinned magnetic domain walls and nucleation sites at these APBs might be explained by a strong AFM coupling between Mn atoms across it [5,13]. Additionally, previous DFT calculations reported an AFM coupling between Mn atoms at $(0,0,0)$ and $(1/2,1/2,1/2)$ sites in the bulk, which are the sites occupied by first-nearest neighbors across the APB [11]. Notice that second-nearest
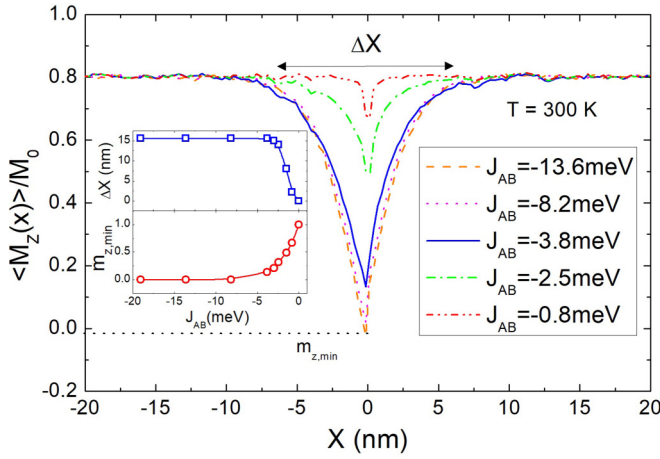
FIG. 14. The spatial average of the magnetization z component $\langle m_z(x) \rangle = \langle M_z(x) \rangle / M_0$ for different exchange coupling strengths across the boundary interface at $T = 300$ K without external magnetic field and demagnetizing field. The inset shows the minimum magnetization z component at the APB $m_{z,\text{min}}$ and the width of the region where the magnetization changes ΔX as a function of the AFM exchange coupling in the APB J_{AB} at $T = 300$ K.

neighbors across the APB are located at distances (4.67 Å) almost twice the separation between the first-nearest Mn atoms (2.62 Å). In Fig. 3 one can see that bulk exchange interactions between neighbors at distances larger than 4.5 Å are quite weak. Bearing all this in mind, as a first approximation, we assume AFM first-nearest-neighbor exchange interactions across the APB, $J_{AB} < 0$, which might be regarded as an effective one. Here, we are especially interested in the relation between the spin dynamics close to the APB and the exchange coupling strength across this defect.

The AFM exchange coupling across the APB leads to a domain wall with one lattice spacing width [see Fig. 12(b)] as the most stable spin configuration (lowest in energy) for all AFM J_{AB} that we considered. However, setting the magnetization of both sides of the APB along the positive direction of the Z axis (easy axis) and relaxing can stabilize another interesting metastable spin configuration shown in Fig. 13. In this case spins across the APB form an angle due to the AFM coupling, and they do not point along the easy axis, reaching a balance between the exchange and anisotropy energies. Strong AFM coupling leads to antiparallel spin alignment on the hard plane XY at the APB. As a consequence, it forms a progressive rotation of spins with opposite chirality. Berger *et al.* reported similar configurations obtained with Monte Carlo simulations in a ferromagnetic cylinder containing an APB [14]. For this kind of spin configuration we initially analyze the mesoscopic magnetization profile at the APB as a function of J_{AB} at room temperature ($T = 300$ K) without external magnetic field and demagnetizing field. Figure 14 shows the spatial average of the magnetization z component $\langle m_z(x) \rangle = \langle M_z(x) \rangle / M_0$ using different exchange coupling strengths across the boundary interface. The inset of Fig. 14 presents the minimum magnetization z component at the APB $m_{z,\text{min}}$ and the width of the region where the magnetization changes ΔX as a function of J_{AB}. We see that $J_{AB} < -10$ meV
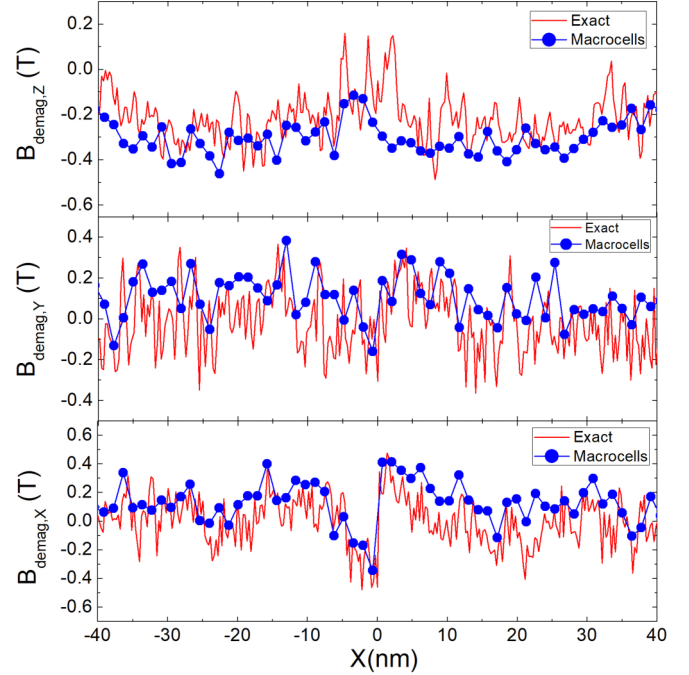

FIG. 15. Demagnetizing field inside of the spin configuration (on spin positions $Y = L_y/2$ and $Z = L_z/2$) shown in Fig. 13 calculated exactly by taking into account all dipole-dipole interactions (red line) and by the macrocell approximation (blue dots).

leads to a region of around 15 nm along the APB where the spatial average magnetization is lower than in the bulk, where the magnetization lies on the hard plane XY just at the APB ($m_{z,\text{min}} \simeq 0$).

Next, we study nucleation and depinning processes, including the demagnetizing field. As pointed out in Ref. [13], a demagnetizing field may play a relevant role close to the APB because it could be sufficient to emit a domain wall. Figure 15 shows a demagnetizing field inside of the spin configuration (on spin positions $Y = L_y/2$ and $Z = L_z/2$) shown in Fig. 13 calculated exactly by taking into account all dipole-dipole interactions and via the macrocell approximation described in Sec. III. We observe that a metastable spin configuration like in Fig. 13 creates a quite uniform demagnetizing field with a z component around 0.3 T pointing opposite the magnetization, which is slightly reduced close to the APB. Switching on the demagnetizing field makes these states quite unstable, especially in the strong-coupling regime ($J_{AB} < -10$ meV) in which the magnetization lies on the hard plane XY at the APB favoring nucleation processes.

Calculated nucleation and depinning fields are shown in Fig. 16(a), while Figs. 16(b) and 16(c) present the spatial average dynamics of the magnetization z component $\langle m_z(x) \rangle = \langle M_z(x) \rangle / M_0$, where $M_0 = M_s(T = 0 K)$, with $J_{AB} = -3.8$ meV in a depinning field of -3.3 T and with $J_{AB} = -2.5$ meV in a nucleation field of -1.2 T, respectively. In the calculation of the depinning field we constrained the spins on the boundaries of the X axis to be along the Z axis, while in the calculation of the nucleation field these spins are not constrained. Including the demagnetizing field decreases depinning and nucleation fields because it favors
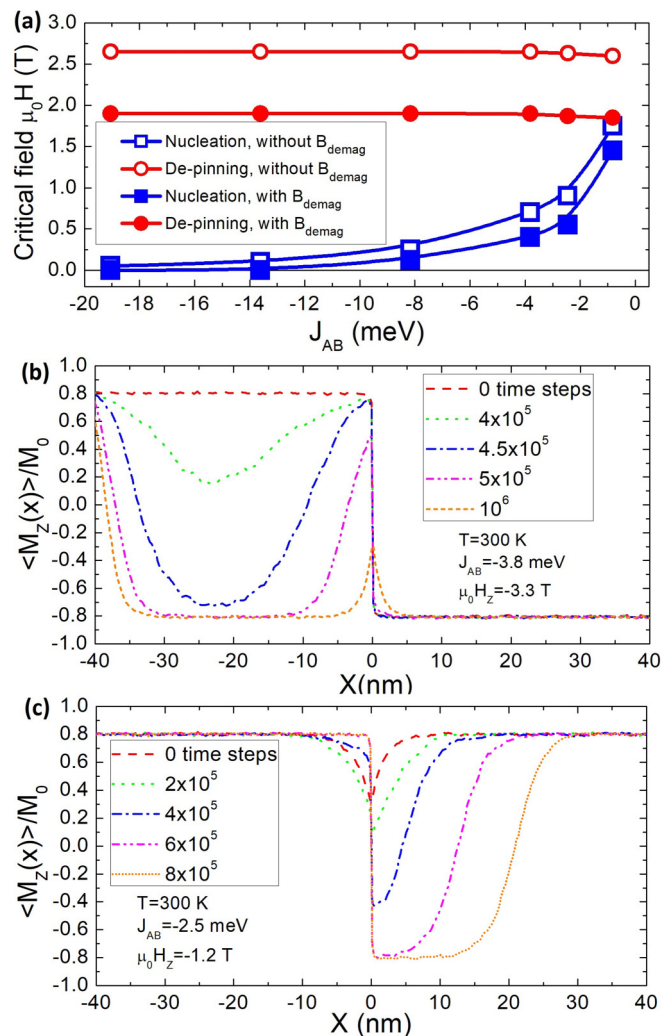
FIG. 16. (a) Calculated minimum fields required for depinning and nucleating a domain wall from an APB as a function of coupling strength J_{AB} across the APB at $T = 300$ K. Open symbols represent calculations without demagnetizing field $\mathbf{B}_{demag}$, while solid symbols stands for calculations including demagnetizing field through the macrocell approximation. (b) Spatial average dynamics of the magnetization z component $\langle m_z(x) \rangle$ with $J_{AB} = -3.8$ meV in a depinning field of 3.3 T and without demagnetizing field. (c) Spatial average dynamics of the magnetization z component $\langle m_z(x) \rangle$ with $J_{AB} = -2.5$ meV in a nucleation field of -1.2 T and without demagnetizing field.

domain wall at the APB it forms a similar spin configuration as the one shown in Fig. 13. Oppositely, nucleation processes in spin configurations like the one shown in Fig. 13 take place close to the APB [see Fig. 16(c)]. These results are in good agreement with recent micromagnetic simulations [15]. Experimental works reported APBs decorated with a domain wall [6–9], suggesting a strong AFM exchange coupling across the APB. According to our ASD results, an effective microscopic exchange coupling $J_{AB} < -10$ meV might be consistent with experimental observations. Finally, metastable spin configurations similar to the one shown in Fig. 13 may also form during the depinning of a domain wall at the APB under strong external magnetic field.

IV. CONCLUSIONS

In summary, in this work we develop an ASD model of the $Mn_{50}Al_{50}$ at.% τ-phase with parameters derived from DFT calculations. The obtained intrinsic properties such as lattice parameters, magnetic moments, magnetocrystalline anisotropy, and exchange integrals are in good agreement with previously reported experimental and theoretical results. From the constructed ASD model we computed the temperature dependence of the magnetization, domain wall width, magnetocrystalline anisotropy, and exchange stiffness, which could be used for a multiscale modeling of this magnet. First-principles calculations of the APB suggest that it might have a short spatial range effect (around four unit cells from the APB) on interatomic distances and atomic magnetic moments.

We also applied this model to study APB phenomena. We calculated critical nucleation and depinning fields as a function of AFM exchange coupling across the APB, as well as the mesoscopic magnetization profile of metastable states. This analysis revealed that an effective microscopic AFM exchange coupling < -10 meV combined with a demagnetizing field could unavoidably form APBs decorated with a domain wall, as always observed in experiment. Finally, we reported possible metastable spin configurations that may also form during the depinning of a domain wall at the APB under strong external magnetic field. We also hope this work can be expanded and improved in the future, including a more accurate description of local exchange interactions and magnetocrystalline anisotropy close to the APB.

The presented ASD model and results might be combined with a micromagnetic approach to design and optimize a microstructure supporting high coercivity on the MnAl τ-phase in the future.

these processes. The depinning field does not depend on the AFM exchange coupling strength at the APB because the depinning of the domain wall is mainly induced by a nucleation which takes place far from the APB, as shown in Fig. 16(b). Here, also notice after the depinning of the

[1] H. Kono, J. Phys. Soc. Jpn. **13**, 1444 (1958).

[2] A. J. J. Koch, P. Hokkeling, M. G. V. D. Steeg, and K. J. de Vos, J. Appl. Phys. **31**, S75 (1960).

[3] J. M. D. Coey, J. Phys.: Condens. Matter **26**, 064211 (2014).

[4] T. Ohtani, N. Kato, S. Kojima, K. Kojima, and Y. Sakamoto, IEEE Trans. Magn. **13**, 1328 (1977).

[5] H. Zijlstra and H. B. Haanstra, J. Appl. Phys. **37**, 1 (1966).

[6] E. L. Houseman and J. P. Jakubovics, J. Magn. Magn. Mater. **31–34**, 1005 (1983).

[7] J. P. Jakubovics, A. J. Lapworth, and T. W. Jolly, J. Appl. Phys. **49**, 3 (1978).

[8] J. Jakubovics and T. W. Jolly, Phys. B (Amsterdam, Neth.) **86–88**, 1357 (1977).

[9] J. van Landuyt, G. van Tendeloo, J. van den Broek, H. Donkersloot, and H. Zijlstra, IEEE Trans. Magn. **14**, 679 (1978).

[10] C. Yanar, V. Radmilovic, W. A. Soffa, and J. M. K. Wiezorek, Intermetallics **9**, 949 (2001).

[11] K. Anand, J. J. Pulikkotil, and S. Auluck, J. Alloys Compd. **601**, 234 (2014).

[12] A. P. Young and J. P. Jakubovics, J. Phys. F: Met. Phys. **5**, 1866 (1975).

[13] H. Zijlstra, IEEE Trans. Magn. **15**, 1246 (1979).

[14] L. Berger, Y. Labaye, O. Crisan, J. M. Greneche, and J. M. D. Coey, J. Appl. Phys. **91**, 7634 (2002).

[15] S. Bance, F. Bittner, T. G. Woodcock, L. Schultz, and T. Schrefl, Acta Mater. **131**, 48 (2017).

[16] N. Kazantseva, D. Hinzke, U. Nowak, R. W. Chantrell, U. Atxitia, and O. Chubykalo-Fesenko, Phys. Rev. B **77**, 184428 (2008).

[17] D. Hinzke, U. Atxitia, K. Carva, P. Nieves, O. Chubykalo-Fesenko, P. M. Oppeneer, and U. Nowak, Phys. Rev. B **92**, 054412 (2015).

[18] B. Skubic, J. Hellsvik, L. Nordström, and O. Eriksson, J. Phys.: Condens. Matter **20**, 315203 (2008).

[19] R. F. L. Evans, W. J. Fan, P. Chureemart, T. A. Ostler, M. O. A. Ellis, and R. W. Chantrell, J. Phys.: Condens. Matter **26**, 103202 (2014).

[20] V. P. Antropov, M. I. Katsnelson, B. N. Harmon, M. van Schilfgaarde, and D. Kusnezov, Phys. Rev. B **54**, 1019 (1996).

[21] J. P. Perdew, K. Burke, and M. Ernzerhof, Phys. Rev. Lett. **77**, 3865 (1996).

[22] K. Lejaeghere, G. Bihlmayer, T. Björkman, P. Blaha, S. Blügel, V. Blum, D. Caliste, I. E. Castelli, S. J. Clark, A. Dal Corso, S. de Gironcoli, T. Deutsch, J. Kay Dewhurst, I. Di Marco, C. Draxl, M. Dułak, O. Eriksson, J. A. Flores-Livas, K. F. Garrity, L. Genovese, P. Giannozzi, M. Giantomassi, S. Goedecker, X. Gonze, O. Grånäs, E. K. U. Gross, A. Gulans, F. Gygi, D. R. Hamann, P. J. Hasnip, N. A. W. Holzwarth, D. Iuşcan, D. B. Jochym, F. Jollet, D. Jones, G. Kresse, K. Koepernik, E. Küçükbenli, Y. O. Kvashnin, I. L. M. Locht, S. Lubeck, M. Marsman, N. Marzari, U. Nitzsche, L. Nordström, T. Ozaki, L. Paulatto, C. J. Pickard, W. Poelmans, M. I. J. Probert, K. Refson, M. Richter, G.-M. Rignanese, S. Saha, M. Scheffler, M. Schlipf, K. Schwarz, S. Sharma, F. Tavazza, P. Thunström, A. Tkatchenko, M. Torrent, D. Vanderbilt, M. J. van Setten, V. Van Speybroeck, J. M. Wills, J. R. Yates, G.-X. Zhang, and S. Cottenier, Science **351**, aad3000 (2016).

[23] G. Kresse and J. Hafner, Phys. Rev. B **47**, 558 (1993).

[24] G. Kresse and J. Hafner, Phys. Rev. B **49**, 14251 (1994).

[25] G. Kresse and J. Furthmüller, Comput. Mater. Sci. **6**, 15 (1996).

[26] G. Kresse and J. Furthmüller, Phys. Rev. B **54**, 11169 (1996).

[27] G. Kresse and D. Joubert, Phys. Rev. B **59**, 1758 (1999).

[28] P. B. Braun and J. A. Goedkoop, Acta Crystallogr. **16**, 737 (1963).

[29] J. H. Huang, P. C. Kuo, and S. C. Shen, IEEE Trans. Magn. **31**, 2494 (1995).

[30] Ph. Kurz, F. Förster, L. Nordström, G. Bihlmayer, and S. Blügel, Phys. Rev. B **69**, 024415 (2004).

[31] M. Ležaić, Ph.D. thesis, Rheinisch-Westfälischen Technischen Hochschule Aachen, 2005.

[32] J. H. Park, Y. K. Hong, S. Bae, J. J. Lee, J. Jalli, G. S. Abo, N. Neveu, S. G. Kim, C. J. Choi, and J. G. Lee, J. Appl. Phys. **107**, 09A731 (2010).

[33] R. Skomski, P. Manchanda, P. Kumar, B. Balamurugan, A. Kashyap, and D. J. Sellmyer, IEEE Trans. Magn. **49**, 7 (2013).

[34] P. C. Kuo, Y. D. Yao, J. H. Huang, and C. H. Chen, J. Magn. Magn. Mater. **115**, 183 (1992).

[35] L. Pareti, F. Bolzoni, F. Leccabue, and A. E. Ermakov, J. Appl. Phys. **59**, 3824 (1986).

[36] UPPASD, http://www.physics.uu.se/research/materials-theory/ongoing-research/uppasd/.

[37] D. Hinzke, U. Nowak, R. W. Chantrell, and O. N. Mryasov, Appl. Phys. Lett. **90**, 082507 (2007).

[38] R. Rothwarf, H. Leupold, J. T. Breslin, A. Tauber, and D. I. Paul, J. Appl. Phys. **52**, 2515 (1981).

[39] S. Zhao, T. Hozumi, P. LeClair, G. Mankey, and T. Suzuki, IEEE Trans. Magn. **51**, 2101604 (2015).

[40] U. S. Ram and P. Gaunt, J. Appl. Phys. **54**, 2872 (1983).

[41] L. Luo, N. Anuniwat, N. Dao, Y. Cui, S. A. Wolf, and J. Lu, J. Appl. Phys. **119**, 103902 (2016).

[42] R. Moreno, R. F. L. Evans, S. Khmelevskyi, M. C. Muñoz, R. W. Chantrell, and O. Chubykalo-Fesenko, Phys. Rev. B **94**, 104433 (2016).